Title

A Rapid Analytical Method for Predicting Injection Rates in Heterogeneous Reservoirs

---

Authors and Affiliations

Arman Darvish-Sarvestani
Department of Earth Science and Engineering
Imperial College London, United Kingdom
Email: a.darvish-sarvestani@imperial.ac.uk

Philip Craig Smalley
Department of Earth Science and Engineering
Imperial College London, United Kingdom

Lidia Lonergan
Department of Earth Science and Engineering
Imperial College London, United Kingdom

Ana Widyanita
PETRONAS Research Sdn. Bhd., Malaysia

Nur Myra Rahayu Razali
PETRONAS Research Sdn. Bhd., Malaysia

Yong Wen Pin
PETRONAS Research Sdn. Bhd., Malaysia

Ann Muggeridge
Department of Earth Science and Engineering
Imperial College London, United Kingdom

Preprint Status Statement

This manuscript is a non-peer-reviewed preprint submitted to EarthArXiv.
The manuscript has been submitted for peer review to the International Journal of Greenhouse Gas Control.

A Rapid Analytical Method for Predicting Injection Rates in Heterogeneous Reservoirs

A. Darvish-Sarvestani[1,*], P.C. Smalley[1], L. Lonergan[1], A. Widyanita[2], N. M. Rahayu Razali[2], Y. Wen Pin[2], A. Muggeridge[1]

[1] Department of Earth Science and Engineering, Imperial College London, UK
[2] PETRONAS Sdn. Bhd., Kuala Lumpur, Malaysia
[*] Corresponding author Email: adarvish@ic.ac.uk

Abstract

Maximum injection rate is a key criterion when screening subsurface hydrocarbon reservoirs or aquifers for possible EOR schemes or storage of hydrocarbon gas, hydrogen or carbon dioxide. It has to be high enough to achieve desired rates without risking the formation fracturing. Screening requires evaluation of thousands or millions of potential injection sites to identify those with favourable characteristics that merit further, more detailed study. This study presents a computationally efficient and geologically informed workflow to rapidly estimate gas injection rates in regional-scale 3D models, combining radial-based permeability upscaling with a transient compressible gas flow model that captures spatial variability in reservoir and fluid properties. The methodology requires an estimate of the distribution of petrophysical properties, pressure and temperature and applies a block-by-block rate calculation scheme, supported by a pre-processing step for pressure-dependent fluid properties (density, compressibility and viscosity). The approach is validated against numerical simulation for the case of geological storage of CO_2 in a saline aquifer and then demonstrated on a real-world regional model covering ~1,200 km^2. Average and maximum errors were 27% and 71% for random heterogeneous cases, and 13% and 30% for field-scale predictions, respectively, demonstrating strong agreement with numerical simulations given the scale and complexity of the models. The full regional model was processed in under five minutes using parallel computing. The key innovation lies in the permeability averaging scheme, which effectively captures near-wellbore heterogeneity for accurate rate prediction without requiring numerical simulation.

Keywords: CO_2 Storage; CCS; Screening; Injection rate; Permeability upscaling; Heterogeneity; Large-scale reservoir modelling.

1. Introduction

A fundamental operational parameter in the design and assessment of subsurface storage and most Enhanced Oil Recovery (EOR) projects is the gas injection rate, where the gas could by carbon dioxide, hydrogen or natural gas. This determines the number and placement of wells, the size of surface facilities, and the overall timescale over which target volumes can be injected. Critically, injection rates must remain within safe bounds to avoid excessive pressure buildup that could compromise caprock integrity or trigger fault reactivation (Birkholzer and Zhou, 2009). Well injectivity is influenced by hydro-physical, chemical, and geomechanical processes—including permeability, fines migration, salt precipitation, and formation damage—especially in the near-well region (Hajiabadi et al., 2021).

Full-physics numerical simulations can provide high-fidelity prediction of injectivity when well-calibrated and finely gridded, but their application in early-stage screening is severely limited by data requirements and computational burden (Celia et al., 2015; Nordbotten et al., 2005). This is especially the case when the goal is to evaluate large numbers of candidate injection sites efficiently and consistently (Zhang et al., 2022). Evaluating thousands—or even millions—of potential injection locations across basin- or region-scale domains is essential to meet gigatonne-scale storage goals. For each candidate site, full simulation would require the construction of local input models and grid files, followed by individual runs, each of which may take hours or days to complete.

Coarse grid simulations are one way to reduce computational time, but these introduce significant numerical errors when calculating injection rate, particularly when Cartesian grids are used. While the Peaceman correction (Peaceman, 1983) compensates for these errors in in the well grid block in homogeneous models, it does not account for heterogeneity in the near well region. In addition standard permeability upscaling is inaccurate when flow is radial (Lake, 1989; Renard and De Marsily, 1997) as occurs in and near the well block. Heterogeneity in the well block and immediately adjacent cells can be represented using methods such as that proposed by Ding (2004). These, however, involve further calculations prior to simulation. In any case even coarse grid simulations become impractical when screening thousands of possible well locations in a single realisation of the subsurface heterogeneity, let alone if multiple alternative geological realisations need to be considered.

Analytical solutions present a faster alternative, yet they are also based on assumptions of homogeneous, isotropic permeability, limiting their applicability in geologically realistic systems with both horizontal and vertical stratigraphic variability, and faulting. Critically, by neglecting heterogeneity in the near-wellbore region, these methods can lead to misleading rate estimates and obscure fair comparison across candidate sites (De Silva and Ranjith, 2012; Smith and Montgomery, 2015; Soeriawinata et al., 1997). Soeriawinata et al. (1997) demonstrated that radial heterogeneity could be partially captured through ray-based distance weighting of permeabilities in a grid-based model,

but their method required manual implementation and did not generalise well to screening workflows.

The estimation of near-well average permeability remains a key uncertainty in such assessments, particularly under radial flow, where small-scale heterogeneity can disproportionately affect rate predictions. The dynamic behaviour of the injected fluid—particularly pressure-dependent viscosity and compressibility of supercritical CO_2—must also be incorporated to obtain physically meaningful rate estimates (Hajiabadi et al., 2021). Existing screening models often ignore these dependencies or rely on steady-state assumptions that break down at high injection pressures or during early-time transients.

To address these limitations, this study introduces a computationally efficient and easy to implement workflow. It combines a radial distance-weighted permeability averaging method with a transient injection model based on Darcy's law for compressible gas. In this work we test and demonstrate the upscaling when screening for geological CO_2 storage in saline aquifers. We evaluate pressure-dependent CO_2 properties using analytical correlations that require only minimal input data, making the approach well suited for basin-scale screening workflows. Similar approaches could be used to estimate gas properties for other subsurface injection scenarios—including gas injection for EOR or storage and hydrogen storage. The workflow can also be applied to screening for processes in which the injection fluids do not have pressure dependent properties such as geothermal reinjection, waterflooding of oil reservoirs and industrial brine disposal operations such as those encountered in potash mining (Krevor et al., 2023; Pumjan et al., 2022).

2. The Workflow

2.1. Overview and Assumptions

The workflow is designed to enable large-scale evaluation of candidate storage sites with minimal data input and without reliance on full-physics numerical simulation. The core objective is to estimate the maximum allowable injection rate accounting for near-well permeability heterogeneity and pressure-dependent fluid behaviour. The method combines (i) a block-based rate prediction framework that aggregates contributions within each stratigraphic interval and geological compartment to represent the effective flow capacity of the near-wellbore region, and (ii) a transient analytical solution based on Darcy's law for compressible gas injection. This combination enables rapid and physically meaningful injection rate estimates across a range of geological settings.

Several assumptions are adopted to maintain analytical tractability while preserving key physical features relevant to the screening stage:

- Radial flow geometry is assumed, which is appropriate for vertical, single-well injection into laterally extensive formations or compartments.

- Vertical equilibrium is not required, but flow is considered predominantly horizontal within each layer.
- Multilayered heterogeneity is captured by calculating the injection rate separately for each grid block (i.e. for every layer within a column) and summing the results to obtain the total well rate. Lateral heterogeneity is incorporated through a radial averaging scheme that accounts for spatial variability in permeability across concentric annuli.
- Capillary, chemical, and geomechanical effects are neglected, in line with the focus on short-term, pressure-driven flow during early injection.
- No-flow boundaries or regional pressure dissipation are not included; the analysis assumes a laterally unbounded reservoir at the screening scale.
- The effect of multiphase flow is simplified through the use of a Corey-type relative permeability function, where the brine saturation is assumed to immediately decline to the irreducible value ($S_w = S_{w,ir}$) within the near-well region upon CO_2 injection.

The workflow requires a static geological model containing mapped reservoir properties (such as reservoir thickness, permeability and porosity distributions), an initial pressure distribution (e.g., estimated from a reference depth using a hydrostatic gradient) and fluid property correlations. These features make it suitable for regional assessments where thousands to millions of candidate locations must be compared consistently and efficiently.

2.2. Transient Injection Model

To estimate the gas injection rate under pressure-limited, transient conditions, a semi-analytical radial flow model is employed (Dake, 1983). The formulation is based on single-phase, isothermal gas injection into a porous medium, and accounts for pressure-dependent viscosity and gas compressibility using a pseudo-pressure formulation. The injection rate, Q_g, in sm^3/s, is computed using:

$$Q_g = \frac{k k_{rg} h (\psi_e - \psi_w)}{T \psi_D} \qquad \textit{Eq. 1}$$

where:

- k = effective permeability (m^2), calculated via the radial upscaling method described in Section 2.2,
- k_{rg} = endpoint relative permeability to the injected gas (dimensionless),
- h = formation thickness (m),
- ψ_w, ψ_e = pseudo-pressure at the external boundary and wellbore, respectively ($Pa^2 \cdot s/m^2$),
- ψ_D = dimensionless pseudo-pressure function that accounts for transient flow effects (dimensionless).

The pseudo-pressure function $\psi(P)$ is defined as:

$$\psi(P) = \int_{P_0}^{P} \left(\frac{2P}{\mu_g Z}\right) dp \qquad \textit{Eq. 2}$$

where:

- P = pressure (Pa),
- μ_g = dynamic viscosity of the injected gas as a function of pressure (Pa·s),
- Z = the gas compressibility factor (dimensionless),
- P_0 = reference pressure (usually zero or initial pressure).

The dimensionless pseudo-pressure function ψ_D is approximated by an analytical solution valid for early- to mid-time radial flow (Dake, 1983):

$$\psi_D = 0.5\,[\ln(\mathrm{t_D}) + 0.80907] \qquad \textit{Eq. 3}$$

The dimensionless time, t_D, is calculated using:

$$t_D = \frac{kt}{\emptyset \mu_g c_t r_w^2} \qquad \textit{Eq. 4}$$

where:

- t = injection time (s),
- $\emptyset$ = porosity (dimensionless),
- μ_g = gas viscosity at average reservoir conditions (Pa·s),
- c_t = total compressibility of the system (Pa^{-1}),
- r_w = wellbore radius (m).

The model assumes radial, horizontal flow in an unbounded reservoir with no capillary, geochemical, or thermal effects. Fluid properties (μ_g, Z) are pressure-dependent and evaluated at each block using the methods described in Section 2.4.

To further reduce computational intensity—particularly during early screening over large spatial domains—the pressure-squared approximation may be used in place of the full pseudo-pressure integral. This simplification assumes that the gas viscosity and compressibility factor remain approximately constant over the relevant pressure range, yielding:

$$\psi(P) \approx \frac{P^2}{\mu_g \mathrm{Z}} \qquad \textit{Eq. 5}$$

While this approach can significantly reduce the need for numerical integration, its applicability is pressure-dependent. It is generally valid only when pressure variation is modest and the injection gas is CO_2 that remains well within the supercritical phase. This will typically be the case at lower to moderate reservoir depths. For CO_2 at higher pressures or over large pressure intervals, and for most other injection gases, deviations in fluid properties can lead to non-negligible error, and the full pseudo-pressure formulation should be retained. In this study, the pressure-squared approximation is not applied unless specifically justified by local conditions.

2.3. Radial Permeability Upscaling

Accurate estimation of injection rates requires realistic representation of the permeability heterogeneity around the well. Traditional averaging techniques (e.g. arithmetic or harmonic means across *ij*-columns) assume linear flow and so are not suitable for the radial flow geometry around a well. In particular, they do not account for the decreasing importance of heterogeneities further from the well.

To address this, an improved radial distance-based upscaling method is implemented that weights each block's contribution according to its distance from the well. The method defines an averaging radius based on a specified number of grid blocks extending radially from the injection point. For each ring of blocks within this radius, a logarithmic weight factor is applied to capture the influence of pressure drawdown across each annulus, consistent with the analytical solution for radial flow in porous media (Ertekin et al., 2001). This approach was inspired by Soeriawinata et al. (1997), but has been improved to remove the need for directional ray-tracing or nested averaging along and across rays.

The effective permeability is then calculated using a weighted harmonic average:

$$k_{av} = \frac{\sum_0^n w_i}{\sum_0^n \frac{w_i}{k_i}} \qquad \textit{Eq. 6}$$

where k_i is the average permeability of blocks within the i^{th} radial band, and $w_i$is its corresponding weight factor. Within each radial band, the permeability k_i is computed as a volume-weighted arithmetic average of the permeabilities of all grid blocks that lie within that annulus. This approach ensures that blocks occupying a larger fraction of the annular volume—due to azimuthal asymmetry or irregular grid geometry—have proportionally greater influence on the final averaged permeability. The use of volume weighting avoids the bias that could arise from simple arithmetic averaging when block sizes are unequal. This detail is illustrated in the caption of Figure 1 and is critical for maintaining consistency with radial flow assumptions in heterogeneous 3D grids. The weight is defined as:

$$w_i = ln\frac{r_i}{r_{i-1}} \qquad \textit{Eq. 7}$$

Here, r_i and r_{i-1} represent the outer and inner radii of the i^{th} annulus, respectively. For the innermost ring ($i = 0$), the inner radius r_{i-1} is equal to the physical wellbore radius r_w, while the outer radius r_0 is defined as the Peaceman equivalent radius r_{eq}, representing the outer boundary of the well-block. This formulation ensures that the influence of each surrounding zone is scaled appropriately, consistent with logarithmic pressure drop theory under radial flow.

The Peaceman equivalent radius defines the effective radial distance from the wellbore centre to the edge of the well-block in a gridded Cartesian model. For non-square grids and anisotropic permeability, it is calculated using the following expression (Ertekin et al., 2001):

$$r_{eq} = 0.28 \frac{\left[\left(k_y/k_x\right)^{0.5}\Delta x^2 + \left(k_x/k_y\right)^{0.5}\Delta y^2\right]^{0.5}}{\left(k_y/k_x\right)^{0.25} + \left(k_x/k_y\right)^{0.25}} \quad \textit{Eq. 8}$$

where:

- Δx, Δy are the gridblock dimensions in the x- and y-directions (m),
- k_x, k_y are the directional permeabilities in the x and y directions respectively (m^2).

This formulation ensures that the equivalent radial distance reflects both the geometry of the grid used to represent the permeability distribution and anisotropy in the permeability tensor.

Figure 1 illustrates the structure of this averaging scheme. The well-block is located at the centre of the grid, and surrounding cells are grouped into five concentric rings based on their radial distance from the wellbore. In practice the total averaging radius (or number of rings *n*) is selected based on the expected near-well influence zone. The logic for selecting this averaging distance — and its impact on predicted permeability — will be further examined in Section 3.2. The well-block equivalent radius (r_{eq}) and the wellbore radius (r_w) are also marked to contextualise their roles in the analytical injection rate formulation.

The radial distance between the injection well and each surrounding grid block, is computed within each layer in the x-y plane. Assuming a Cartesian coordinate system and uniform grid spacing ($\Delta x = \Delta y$), the radial distance r_{ij} from the centre of the injection well-block located at index $(i,\ j)$ to any other block at index $(i_1,\ j_1)$ in the same layer is given by:

$$\text{Distance} = \Delta x \sqrt{(i - i_1)^2 + (j - j_1)^2} \quad \textit{Eq. 9}$$

In models with non-uniform grid spacing, the distance is calculated directly from the wellbore centre to the centroid of each target block.

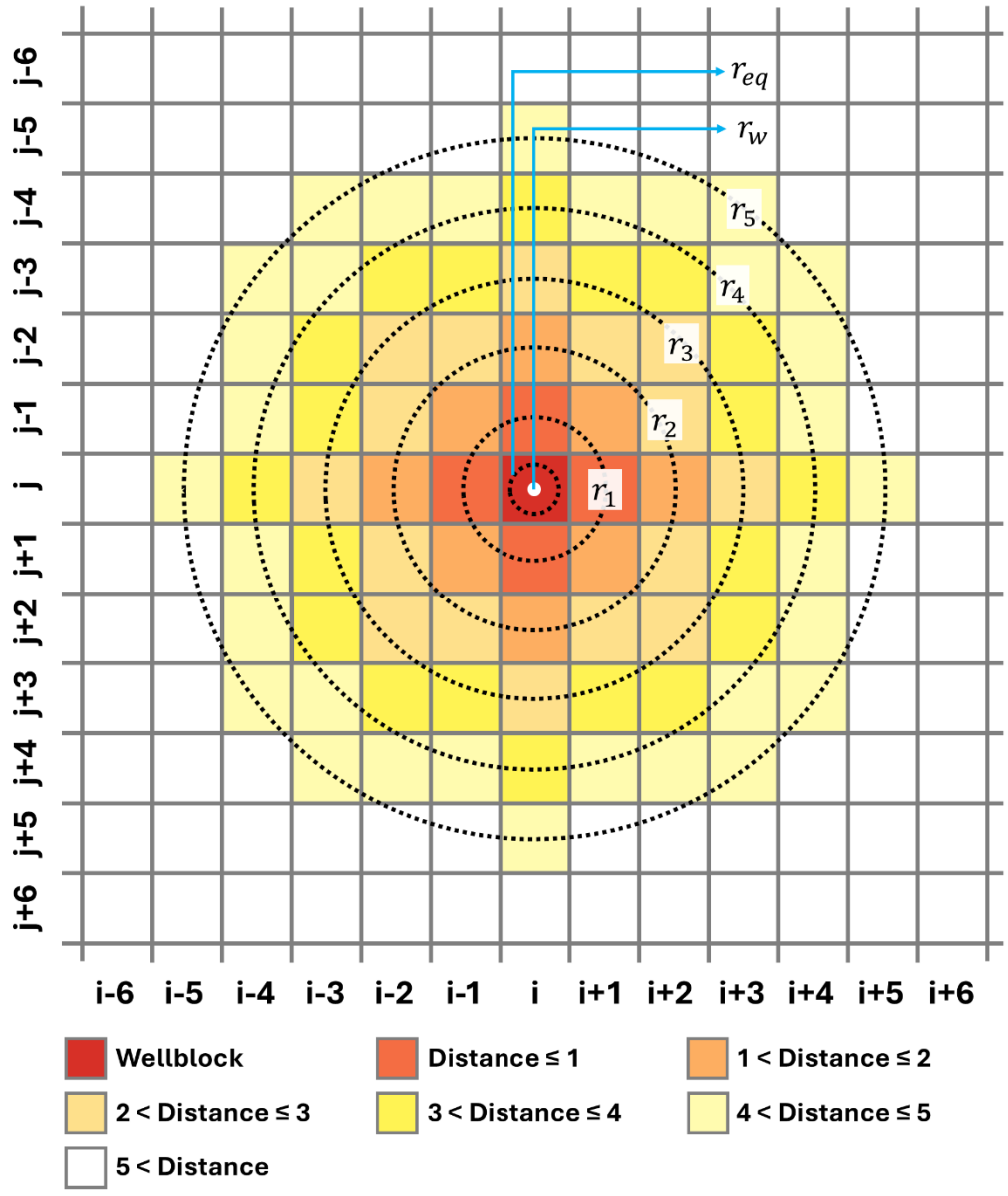

Figure 1 Schematic illustration of the radial permeability averaging method. The injection well is located at the centre of the well-block (i, j), and surrounding grid cells are grouped into concentric rings based on their radial distance from the wellbore. Each coloured annulus represents an incrementally larger radial band, with weights decreasing outward to account for reduced flow influence. In uniformly gridded models (Δx = Δy), the distance from the wellbore to each surrounding block can be expressed in discrete grid units. The concentric black dashed circles delineate the boundaries of each averaging ring (r_{eq}, r_1-r_5). The effective averaging radius in this example is 1 km, corresponding to five 200 m-wide grid blocks. This configuration defines the near-well region over which permeability is averaged in the proposed upscaling method.

239 This permeability upscaling is applied for each unique potential injection location in the
240 model. Cells on the opposite side of sealing faults are excluded from the averaging
241 region.

2.4. Fluid Property Estimation

Accurate estimation of pressure-dependent fluid properties is essential for computing gas injection rates. In practical applications, it is likely that the initial pressure will vary across the region due to compartmentalization and/or variations in formation depth (e.g. dip or structural relief), the structure of the formations of interest, and any hydrocarbon fields or pre-existing storage schemes. This means that the gas compressibility factor Z and the dynamic viscosity μ_g, have to be evaluated locally for each grid block using input pressure and temperature fields from the geological model.

This study demonstrates the workflow for the screening of potential supercritical CO_2 injection sites in a saline aquifer. We calculate the compressibility factor Z using the Peng–Robinson equation of state (PR EoS), which captures non-ideal gas behaviour across a wide range of pressures and temperatures (Ali et al., 2014; Dall'Acqua et al., 2017; Xiong et al., 2024). The EoS is applied directly to each grid block using local temperature and pressure fields provided by the static reservoir model, enabling consistent integration with the pseudo-pressure formulation described in Section 2.2. The CO_2 viscosity is calculated using an empirical correlation derived from Table 8 of Naghizadeh et al. (2022). Since all reservoir temperatures in this case study exceed 300 K, only the high-temperature portion of the correlation is applied. The formulation is implemented in a standalone MATLAB routine and applied locally for each block across the 3D domain.

To verify the accuracy of fluid property estimation, predictions were compared against reference values from the NIST CO_2 property database (National Institute of Standards and Technology (NIST)). The comparison was performed across a broader pressure range but showed good agreement within 15–60 MPa and 340–460 K, which aligns with the operating envelope of most CCS storage projects. Within this range, the model demonstrated good agreement with NIST data, with errors generally within ±5% and no systematic deviation observed. The model has not been validated outside this range.

This property estimation framework ensures both physical reliability and computational efficiency, making it well suited for high-throughput injection rate prediction in basin- and region-scale geological CO_2 storage studies.

2.5. Implementation Workflow for Screening Purposes

The proposed injection rate prediction method is implemented in MATLAB and designed for efficient application to 3D geological models exported from static modelling software such as Petrel. The full workflow is modular and accounts for fault compartmentalisation by recognising predefined flow compartments: only grid blocks within the same compartment as the injection well are included in the calculation, while blocks isolated across sealing faults are excluded. This ensures hydraulic consistency in regional-scale screening studies.

To apply this workflow, a static geological model with petrophysical properties (e.g., porosity and permeability) must be available, along with initial pressure and

temperature values at the datum depth for each stratigraphic interval. These datum conditions are sufficient to construct pressure and temperature profiles across the model domain using simple depth-based interpolation, allowing for consistent fluid property estimation. Additionally, pre-screening can be performed prior to rate prediction to exclude unsuitable locations — for example, cells associated with hydrocarbon-bearing formations, surface infrastructure constraints, or insufficient caprock integrity — ensuring that only technically viable injection locations are considered.

A detailed description of each implementation step and the corresponding workflow diagram are provided in Appendix A: Step-by-Step Workflow for Injection Rate Prediction.

3. Flow Rate Validation

The calculation of gas injection rate is first compared against numerical simulation for CO_2 injection into a saline aquifer using radial and Cartesian grids. CMG-GEM was used for all numerical simulations

3.1. Homogeneous Model Description

To validate the proposed analytical workflow, a series of synthetic numerical models was constructed and simulated under controlled conditions. These models were designed to isolate the impact of grid geometry and resolution on the predicted injection rates, allowing for a direct comparison between analytical and numerical solutions. Two distinct grid types were used for this validation: radial and Cartesian. Table 1 summarises the grid specifications, total domain sizes, and cell counts for each synthetic case.

First the results from simulations in a homogeneous radial grid were compared against the analytical solution. Radial grid results should match the analytical solution, provided there is sufficient grid resolution, as this type of grid minimises discretization and grid orientation error.

The Cartesian models, on the other hand, will not agree with the analytical model, no matter how fine the mesh, due to grid orientation error. The purpose in this case was twofold: first, to evaluate the magnitude of this error in more typical coarse-grid configurations used in screening studies, and second, to assess the impact of grid resolution. All Cartesian grids were constructed using uniformly sized blocks and a square domain of similar lateral extent (~12.5 km × 12.5 km). Three block sizes (50 m, 100 m, and 200 m) were used for analysing the effect of averaging distance. Finer (5 m and 20 m) and coarser (500 m) Cartesian models were included to evaluate the impact of grid resolution on numerical predictions.

Across all simulations, fluid and reservoir properties were selected to remain consistent between the analytical model and numerical simulations. The Peng–Robinson equation of state (PR EoS) was applied in all cases to ensure realistic behaviour of supercritical

CO_2, and care was taken to ensure comparable Z-factors, viscosities, and compressibilities between the numerical simulator and analytical model across the tested pressure range. The porosity was set to 0.15 in all models. Four permeability values were tested: 9.869×10^{-17} m^2 (0.1 mD), 9.869×10^{-16} m^2 (1 mD), 3.454×10^{-15} m^2 (3.5 mD), and 9.869×10^{-15} m^2 (10 mD), representing a range from tight to moderately permeable formations. For each permeability, simulations were run at two formation thicknesses (1.52 m and 6.10 m) and two injection pressure conditions, corresponding to pressure differences of approximately 6.0 MPa and 8.7 MPa (i.e., injection pressures of 20.7 MPa and 23.4 MPa, respectively). In the numerical simulations, a Corey-type gas–water relative permeability function was used, with an initial brine saturation of 0.16 (irreducible water saturation, $S_{w,ir}$) assigned to the injection cell to represent immediate drainage. In the analytical model, the same endpoint values were applied for consistency: S_w was fixed at $S_{w,ir} = 0.16$ and the corresponding maximum gas relative permeability $k_{rg,max} = 0.74$ was used. While this simplification omits the smooth transition captured by Corey curves, it preserves the same limiting behaviour as the numerical model and significantly reduces computational complexity for screening applications.

Table 1 Summary of Synthetic Grid Configurations Used for Model Validation.

Model Type	Grid Dimensions	Block Size (m)	Domain Size (m × m)	Total Cells	Notes
Radial Grid	35 × 20 × 1	Variable (0.15 m to 1,340 m)	~12,192 m radius (40,000 ft dia.)	700	Logarithmic radial spacing
Cartesian (5 m)	2,491 × 2,491 × 1	5 × 5	12,455 × 12,455	6,205,081	Used to assess grid resolution impact
Cartesian (20 m)	631 × 631 × 1	20 × 20	12,620 × 12,620	398,161	Used to assess grid resolution impact
Cartesian (50 m)	249 × 249 × 1	50 × 50	12,450 × 12,450	62,001	Also used for averaging distance analysis and grid resolution sensitivity
Cartesian (100 m)	125 × 125 × 1	100 × 100	12,500 × 12,500	15,625	Also used for averaging distance analysis and grid resolution sensitivity
Cartesian (200 m)	63 × 63 × 1	200 × 200	12,600 × 12,600	3,969	Also used for averaging distance analysis, grid resolution sensitivity and analytical–numerical comparison
Cartesian (500 m)	25 × 25 × 1	500 × 500	12,600 × 12,600	625	Used to assess grid resolution impact

We assumed an initial pressure of 14.7MPa in all cases. The injection rate from the numerical simulations was determined at 31 days at early injection time, prior to pressure boundary influence. This time was chosen based on inspection of pressure profiles across the domain, which confirmed negligible boundary effects within this early period across all homogeneous test cases. These rates were converted from sm^3/s to mass flow rate in mega-tonnes per year (Mt/yr) using a CO_2 density of 1.8567 kg/m^3 at standard conditions (1 atm, 60°F). This ensures a consistent mass-based comparison between analytical and numerical results.

3.2. Sensitivity to Averaging Radius and Permeability Variability

The aim of this sensitivity study was to determine the minimum radial averaging distance needed in a Cartesian grid. This was determined by comparing the rates from the heterogeneous simulations with those predicted from the analytical solution using the upscaled permeability. Three different well-block permeabilities were tested: 0.1 mD, 1 mD, and 10 mD, representing a range from tight to moderately permeable formations. For each permeability distribution, we used the same three grid resolutions as in the homogeneous runs.

The different heterogeneity realizations were created by keeping the injection cell and a varying number of surrounding cells at their original value, but varying the permeability of the remaining cells more distant from the well by 2–3 orders of magnitude. For example, in one case only the injection cell retained the original permeability, while in others, all blocks within a radial distance of 1 to 28 blocks (i.e. up to ~1.4 km) from the wellbore retained the original value, and the remaining cells were altered. To evaluate the robustness of the upscaling and integration methodology under heterogeneous conditions, 57 single-layer Cartesian models were constructed with varied permeability distributions. These included both structured trends (e.g. permeability increasing or decreasing radially from the well) and fully random spatial heterogeneity across a wide permeability range (0.01–1000 mD). This design ensured coverage of a broad spectrum of geologically realistic variability, testing the method's applicability to diverse subsurface conditions.

To determine the minimum radial distance required for reliable permeability upscaling, a series of tests were conducted using different averaging radii centred on the injection cell. For each model, only the cells within the specified radius retained their original permeability values, while the remainder were assigned contrasting values to introduce heterogeneity. The averaging distance was incrementally increased in steps of 50 m, 100 m, and 200 m for the 50 m, 100 m, and 200 m Cartesian grid models, respectively, extending up to approximately 12 km in the largest cases (Table 2). For lower-permeability models, averaging distances between 0 and approximately 1.5 km were systematically evaluated, whereas for higher-permeability cases, the investigated averaging distance was adaptively defined based on the optimal distances identified in preceding tests. The resulting upscaled permeability was used in the analytical model, and predicted rates were compared against those from the numerical simulation. This enabled assessment of the minimum upscaling radius needed to capture heterogeneity

effects without calibrating between methods. For each test case, the predicted rate was directly compared with its counterpart in CMG-GEM using the same underlying permeability distribution. A summary of configurations tested is provided in Table 2.

Table 2 Summary of Radial Averaging Sensitivity Test Cases Used for Heterogeneous Models.

Model Type	Averaging Radii Tested (m)	Number of Cases	Notes
Cartesian (50m)	50, 100, 150, ..., 12000	25 - 30	Increased in 50 m steps up to ~12 km; range refined according to permeability.
Cartesian (100m)	100, 200, 300, ..., 12000	15 - 20	Increased in 100 m steps; range refined according to permeability.
Cartesian (200m)	200, 400, 600, ..., 12000	5 - 10	Increased in 200 m steps; range refined according to permeability.

Results, summarised in Figure 2, show that as block size increases, a larger averaging distance is required to compensate for coarse discretisation and heterogeneity. For instance, with 200 m blocks, at least a 1 km averaging radius is needed to stabilise the upscaled permeability for typical injection-rate predictions. In contrast, finer grids (e.g. 50 m blocks) achieve similar accuracy with averaging radii as small as 200–300 m. Importantly, the effect of block permeability is nonlinear; higher-permeability cases require longer averaging distances to adequately capture connected flow pathways across the model domain.

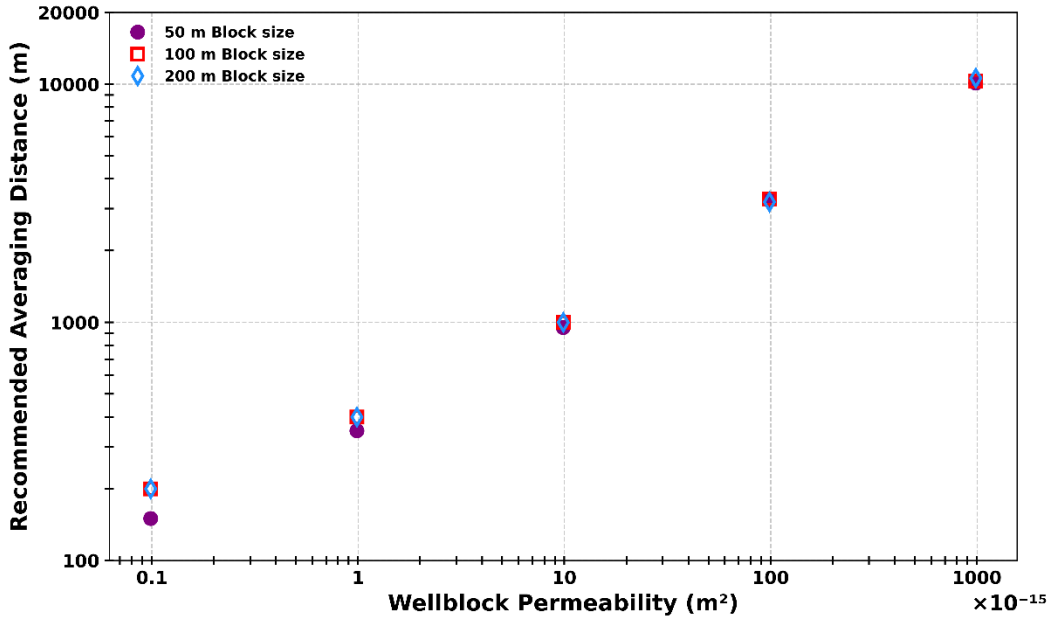

Figure 2 Recommended radial averaging distance for permeability upscaling as a function of well-block permeability and grid resolution. Results are based on synthetic simulations with homogeneous and heterogeneous distributions, showing the minimum averaging distance required to achieve consistent injection rate predictions across three different block sizes

(50 m, 100 m, and 200 m). Well-block permeability is shown in SI units (m^2), corresponding to 0.1, 1, 10, 100, and 1000 mD, respectively.

3.3. Homogeneous Model Results and Grid Sensitivity

The comparison of analytical predictions against numerical simulation results for the homogeneous test cases (Figure 3-Figure 5) shows that numerical simulation consistently underestimates the transient gas injection rate even when using radial grids. This deviation is not a result of input inconsistencies, as all models share identical reservoir and fluid properties.

The underestimation observed in radial models is attributed to the inherent spatial averaging within the simulation grid and numerical dissipation near the wellbore. Despite using logarithmically spaced blocks to improve resolution in the near-field region, the numerical model still cannot fully capture the sharp pressure gradients assumed by the analytical solution, particularly at early times. All simulations were run using a minimum time step of 10^{-3} days (2.4×10^{-2} hours) to ensure accuracy during early transient flow (Sammon, 1988). This results in injection rates that are consistency lower than their analytical counterparts at the selected comparison time (31 days or 744 hours). The comparison time of 31 days was selected to ensure that the initial transient effects had sufficiently developed while still remaining within the early-time regime, where boundary influences are negligible and the analytical solution remains valid. As shown in Figure 3, numerical rates remain lower than analytical predictions throughout the injection period, including very early times.

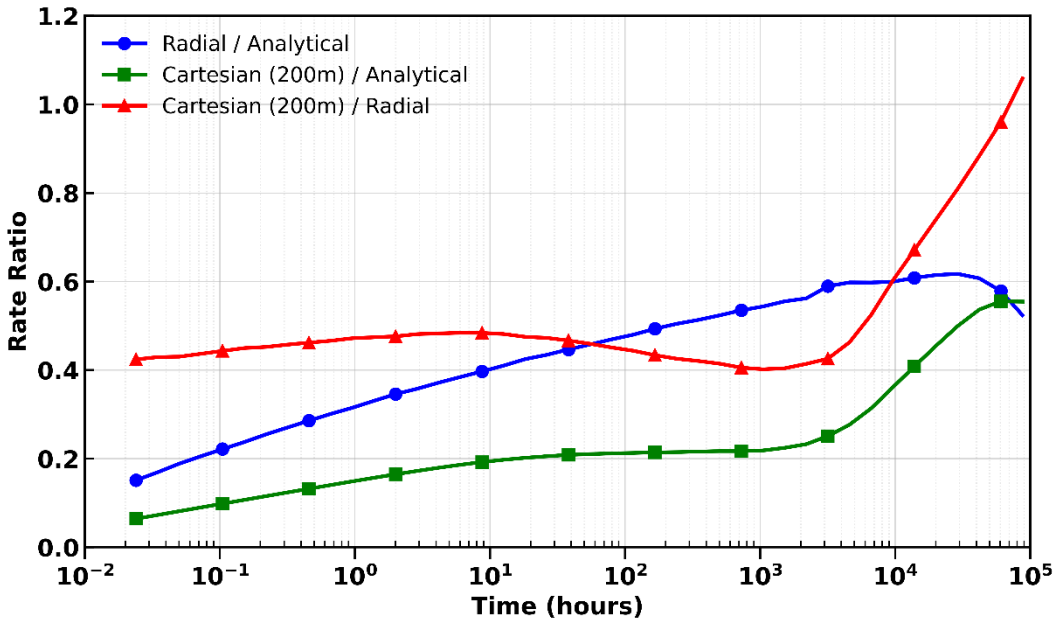

Figure 3 Evolution of injection-rate ratios over time for radial and Cartesian coarse-grid (200 m × 200 m) models. Curves show both the numerical-to-analytical rate ratio and, for reference, the Cartesian-to-radial numerical rate ratio. Results are based on homogeneous models with a permeability of 9.869×10^{-15} m^2 (10 mD), a thickness of 1.52 m, and a constant injection pressure of 20.7 MPa. Despite using a minimum time step of 10^{-3} days (0.024 hours),

numerical rates remain consistently lower than analytical predictions, primarily due to spatial discretisation and geometric limitations in the numerical grid.

The discrepancy is more pronounced in Cartesian coarse-grid models, where the uniform block size (200 m × 200 m) limits resolution around the injection cell. These models significantly underestimate the flow rate compared to both the analytical solution and the radial-grid simulations. The effect is geometric in nature and independent of permeability distribution or pressure conditions. To further evaluate this effect, a sensitivity analysis was conducted across a range of Cartesian grid resolutions (5 m to 500 m), as shown in Figure 4. The results indicate that the underestimation is reduced with finer grid resolution, but a noticeable gap remains even at 5 m resolution. This suggests that further grid refinement yields diminishing returns and cannot fully capture the early-time sharp gradients assumed in the analytical model.

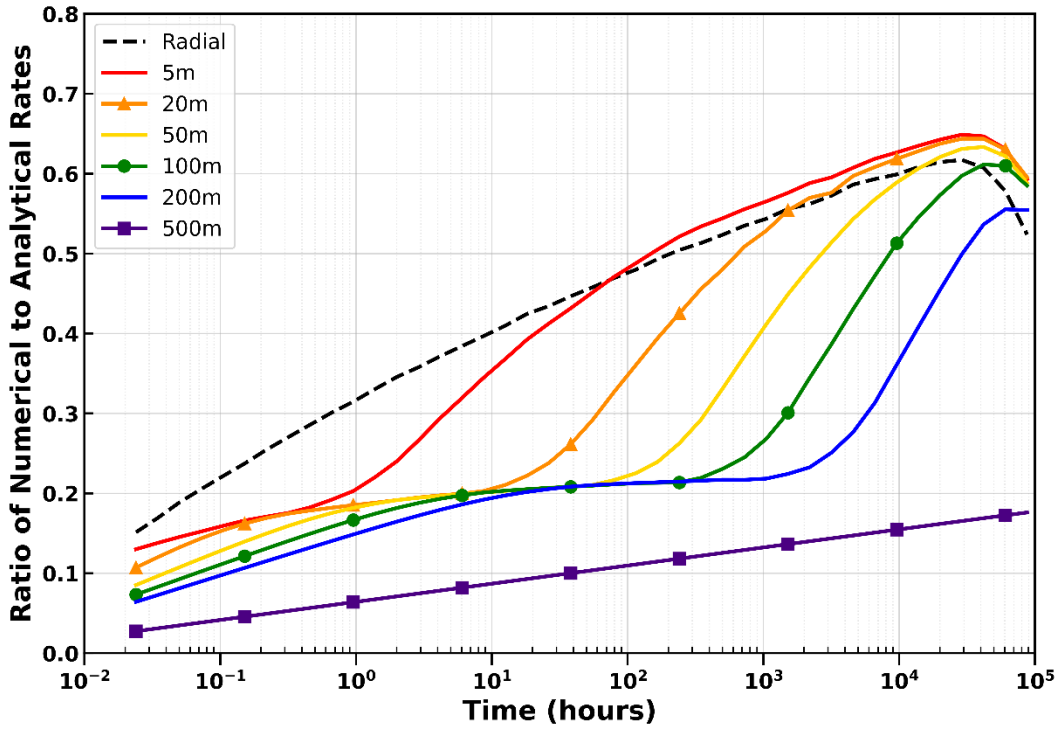

Figure 4 Effect of Cartesian grid resolution on numerical-to-analytical injection rate ratio over time. Results are based on homogeneous models with permeability of 9.869 × 10^{-15} m^2 (10 mD), thickness of 1.52 m, and a constant injection pressure of 20.7 MPa. Finer grids improve early-time agreement with the analytical solution, but a consistent underestimation remains even at 5 m resolution due to spatial averaging and pressure dissipation near the wellbore.

These results highlight the importance of accounting for grid sensitivity when comparing analytical predictions to numerical benchmarks. Temporal and spatial resolution tests (Figure 3 and Figure 4) confirm that the observed underestimation arises from grid resolution effects rather than inconsistencies in the analytical solution. Therefore, the analytical predictions are taken as the reference, and a systematic correction factor was derived from the relationship between analytical and coarse-grid (200 m) numerical simulation results (Figure 5). This correction was then applied to the coarse-grid

numerical results before comparison in heterogeneous models, ensuring a fair and consistent basis for validation (e.g. Figure 6).

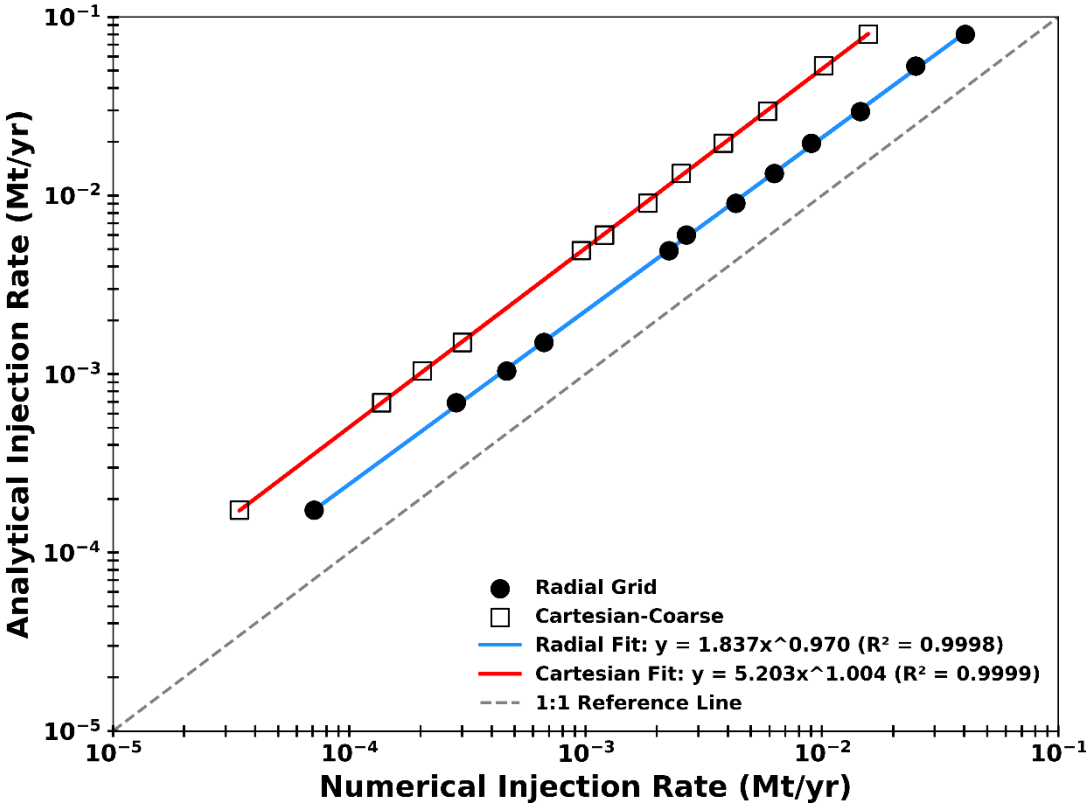

Figure 5 Comparison between analytical injection rate predictions and numerical simulation results for 12 homogeneous single-layer models with different assigned permeabilities. Results from radial-grid simulations (filled circles) and coarse Cartesian-grid simulations (open squares) are plotted against the corresponding analytical predictions. All models use identical fluid and reservoir conditions. A 1:1 reference line is included alongside best-fit power-law regression curves for each numerical dataset. Numerical simulations using both grid types underestimate the injection rate relative to the analytical solution, with the deviation being more pronounced for the Cartesian coarse-grid models due to discretization errors.

3.4. Heterogeneous Model Results

The performance of the proposed analytical method when using the improved upscaling approach (section 3.2) for heterogeneous reservoir conditions is illustrated in Figure 6. This compares analytically predicted injection rates to those obtained from CMG-GEM numerical simulations on a Cartesian coarse grid, after applying the empirical correction derived in Figure 5.

Plotted on a log–log scale, the figure includes a 1:1 reference line and a best-fit linear regression through the numerical data. The resulting correlation is strong, with an R^2 value of 0.9806, demonstrating that the analytical approach remains robust across a wide range of geological variability.

While the predictions cluster closely around the 1:1 line, deviations naturally increase in cases with extreme heterogeneity or near-wellbore flow restrictions. The maximum observed error reached 71.2%, while the average absolute error across all cases was 27.1%. Importantly, screening evaluations rely chiefly on the relative ranking of potential injection sites rather than on absolute rate accuracy. In these heterogeneous models, the prediction errors are largely systematic rather than random, meaning that higher- and lower-performing locations remain correctly differentiated. Despite the variations in absolute error, the method therefore preserves the relative performance hierarchy required for high-level screening studies.

These findings confirm that the analytical model provides a reliable and computationally efficient means of estimating injection rates across complex reservoir conditions. When the numerical simulation results are appropriately corrected for grid geometry and resolution effects (as established in the homogeneous tests), they align with the analytical solution, offering a practical alternative to full-physics simulation in large-scale screening workflows.

These findings provide practical guidelines for selecting the spatial averaging distance during permeability upscaling for injection rate estimation.

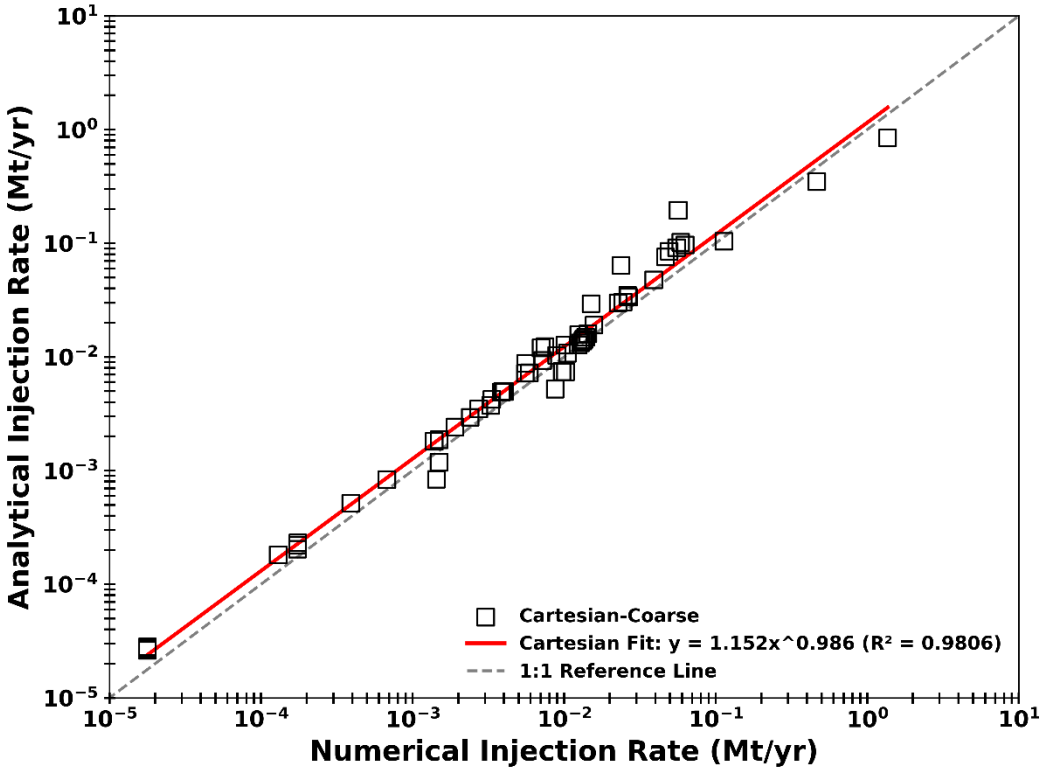

Figure 6 Validation of the analytical injection rate predictions against empirically corrected numerical simulation results for 57 heterogeneous single-layer models with coarse Cartesian grid (200 m × 200 m). Each point corresponds to a distinct permeability distribution, including 20 structured cases with controlled spatial variation and 37 randomly generated cases (ranging from 0.01 mD to 1000 mD, or 9.869×10^{-18} to 9.869×10^{-13} m^2). A strong correlation is observed between analytical and numerical predictions despite local flow deviations caused by heterogeneity. The fitted power-law regression (red) exhibits high accuracy (R^2 = 0.9806). The grey dashed line represents the 1:1 reference line.

3.5. Observed Limitations and Applicability

The validation results discussed in Sections 3.3 and 3.4 confirm that the proposed analytical workflow can provide reliable estimates of pressure-constrained injection rates under a range of geological conditions. Nonetheless, the method is based on a number of physical and geometrical assumptions that define its domain of applicability and inform its limitations.

A key assumption is that flow around the wellbore is approximately radial, particularly within the individual compartments and intervals defined in the geological model. While the presence of faults, baffles, or other large-scale heterogeneities could in principle distort the radial symmetry of the pressure field, this challenge is explicitly addressed in the implementation through compartmental segmentation. To preserve radial flow behaviour and avoid geomechanical risks, blocks located within the permeability averaging distance from sealing faults are excluded from injection rate calculations. This ensures that only hydraulically connected and geomechanically suitable regions contribute to the total injection rate estimate. This preserves the physical validity of the radial assumption within each segment, even in geologically complex systems.

The model does not capture large-scale directional pressure gradients or regional boundary effects that may influence long-term pressure build-up. It assumes a laterally unbounded system at the screening scale, which is appropriate for early-time, short-duration injection assessments, but may not reflect long-term basin-scale behaviour or pressure interference between injection wells.

The methodology also assumes rapid displacement of brine in the near-wellbore region upon injection onset. A residual water saturation is imposed immediately within the analytical model using Corey-type relative permeability curves, with a maximum gas relative permeability of 0.74. This simplification is intended to mimic the initial water drainage process and maximise CO_2 mobility near the well. The method also neglects more complex multi-phase flow interactions, such as water–CO_2 phase interference, which are generally of secondary importance during early-time injection. Hysteresis is not expected to occur during ongoing injection and is therefore not explicitly represented. While this assumption is reasonable for many high-permeability saline formations, it may overpredict injectivity in tighter intervals or capillary-dominated systems where drainage proceeds more slowly.

Importantly, the method does not account for geomechanical stress responses, which may become more significant under high-rate or long-term injection conditions. Other near-wellbore processes such as skin effects, salt precipitation (dry-out), and non-Darcy flow are also not represented; these could be incorporated if needed but are best addressed through more detailed, site-specific studies. Despite these limitations, the proposed workflow provides a practical, computationally efficient means for evaluating near-well flow capacity and screening large numbers of candidate sites. Its ability to integrate realistic permeability heterogeneity, stratigraphic layering, and compartmentalisation while maintaining analytical tractability makes it particularly

well-suited to regional storage assessments, regulatory scoping studies, and portfolio-level ranking of prospective injection locations.

4. Field-Scale Application in a Regional 3D Model

4.1. The Regional Model

To evaluate the applicability of the proposed injection rate prediction workflow under realistic geological conditions, the method was applied to a regional-scale 3D geological model covering approximately 45 km × 26.6 km laterally. The model consists of 226 × 133 × 230 blocks, where each grid cell has a uniform horizontal resolution of 200 m × 200 m. The vertical layering comprises 230 layers grouped into nine stratigraphic intervals, with individual layer thicknesses ranging from 0.08 m to 18.56 m. The overall depth of the model spans from 1,246 m to 2,406 m, reflecting the geological variation across the domain. The model represents a structurally complex region within the Malay Basin, Southeast Asia, characterised by multiple fault blocks, legacy wells, and coexisting hydrocarbon fields and saline aquifers — making it a representative test case for regional-scale CCS screening workflow.

The geological model comprises nine stratigraphic intervals, each representing a distinct depositional system with varying petrophysical properties. To illustrate the methodology, we focus on one interval interpreted as a lower coastal plain to marginal-marine system dominated by low-energy overbank and floodplain deposits, interbedded with channel sands and laterally extensive shoreface–mouth bar sands (Figure 7). Each interval is structurally segmented into four compartments due to post-depositional faulting, rather than depositional boundaries—particularly across three hydrocarbon fields. While the results presented here focus on this illustrative interval, the analytical method was rigorously validated across all nine depositional environments, including fluvio-deltaic, shoreface–mouth bar, deep-water slope channel, and low-energy coastal plain systems. One field (F1) is consistently divided by sealing faults into two isolated compartments. In total, the model includes 36 unique flow segments, corresponding to four structural compartments per interval. Hydrocarbon presence is confined to localised areas within selected stratigraphic intervals, as shown in Figure 8Maximum well rates were estimated for all grid blocks using the workflow described in Section 2.5 and **Appendix** A: Step-by-Step Workflow for **Injection** Rate Prediction, under the general assumptions outlined **in** Section 2. In addition, , which illustrates mapped fault-bounded gas accumulations and their spatial extent. Of the 36 intervals, 25 contain confirmed hydrocarbon zones, based on prior geological and reservoir characterisation.

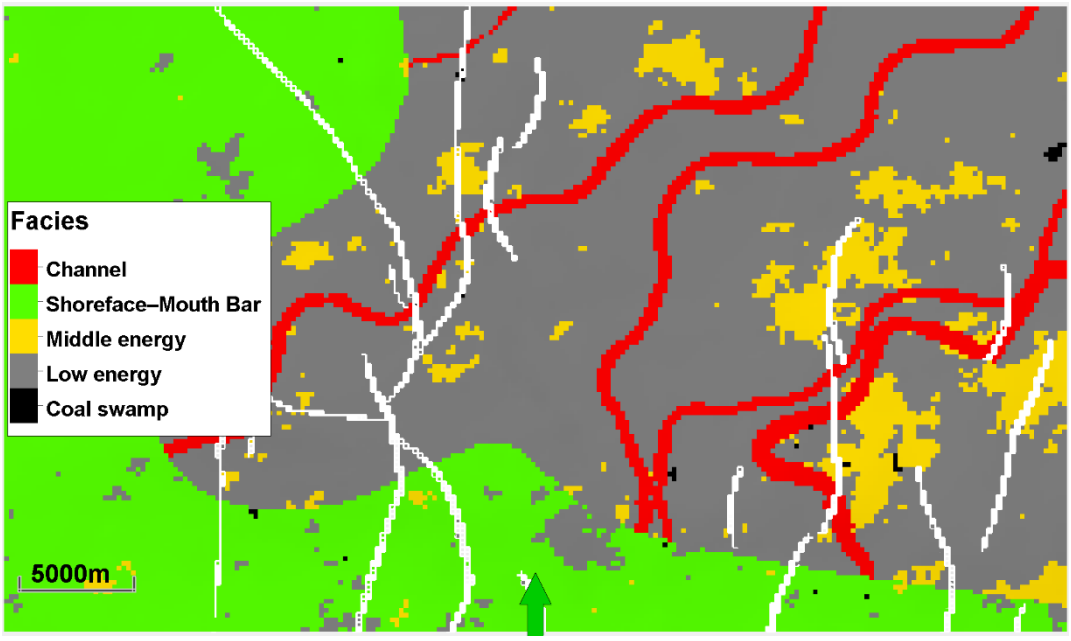

Figure 7 Facies map of the example interval used to demonstrate the analytical workflow. This interval represents a lower coastal plain to marginal-marine depositional system, characterised by low-energy overbank and floodplain deposits (grey), narrow high-sinuosity channel sands (red), and laterally extensive shoreface–mouth bar sands (green) with net-to-gross ratios close to 1. Middle-energy sand bodies (yellow) and coal swamp deposits (black) occur locally. White lines indicate post-depositional faults that structurally segment the interval into four compartments.

The maximum allowable injection pressure in each well-block is constrained by a geomechanical failure criterion. Specifically, the pressure increase above initial reservoir pressure is limited to 90% of the estimated fracture pressure, consistent with conservative regulatory practices (EPA, 2010). For the illustrated interval, the initial reservoir pressure ranges from 13.4 to 22.8 MPa, the maximum allowable injection pressure ranges from 22.1 to 36.9 MPa, and the corresponding allowable pressurisation is between 8.7 and 14.1 MPa. This limit is estimated using input data on rock strength, stress state, and depth, and is based on a stress-based formulation adapted from fracture pressure constraints. This is purely for illustration – in practice the engineer may choose to undertake a more sophisticated calculation of the fracture pressure.

Maximum well rates were estimated for all grid blocks using the workflow described in Section 2.5 and Appendix A: Step-by-Step Workflow for Injection Rate Prediction, under the general assumptions outlined in Section 2. In addition, four potential well-blocks from the selected interval and a further 16 potential well-blocks distributed across other intervals were used to validate the method's general applicability and to compare estimates with those obtained using the upscaling approach of Soeriawinata et al. (1997).

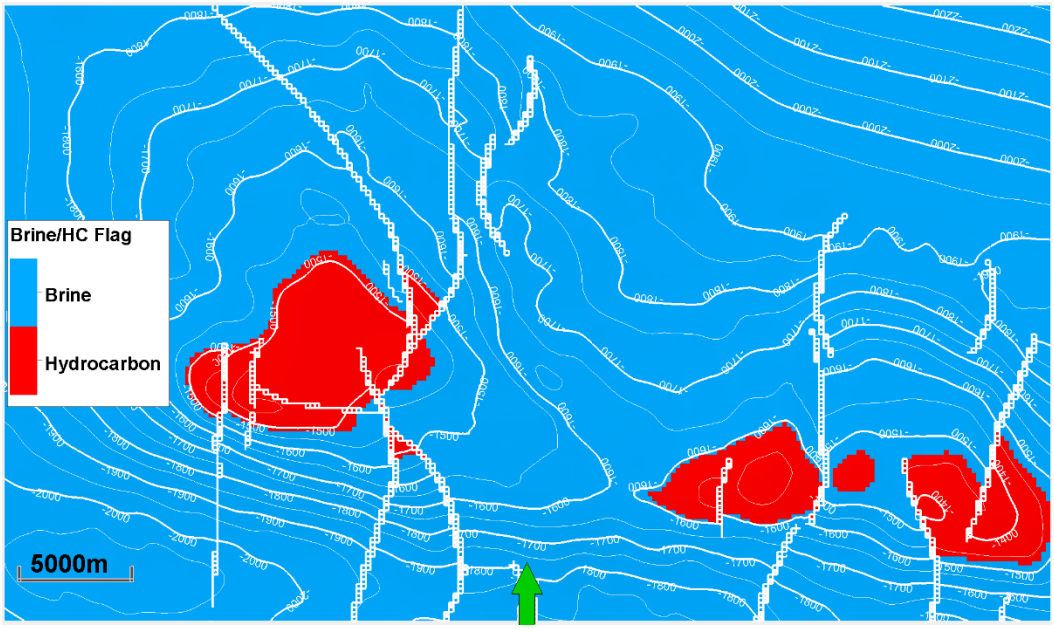

Figure 8 Structural depth map (top reservoir) for a representative interval within the regional 3D geological model. Depth contours (in metres TVDSS) are shown in blue, while mapped fault traces are overlaid in white. Red-shaded areas indicate hydrocarbon-bearing regions as defined in the static model. The map demonstrates the presence of multiple structurally isolated compartments and highlights that hydrocarbon occurrences are confined to limited areas within each interval.

4.2. Results

Figure 9 and Figure 10 show the results for the illustrated interval. The injection-rate maps in Figure 10 are computed for every valid block in the interval, providing continuous spatial coverage. The four test wells shown are a subset of the 20 randomly selected candidate locations used to validate the analytical rate predictions against detailed numerical simulation (CMG-GEM) across the regional model. They are included here only as visual reference points and are not used to generate the maps themselves. Figure 9a shows the original permeability distribution, and Figure 9b presents the corresponding averaged permeability field obtained using the proposed radial upscaling approach. The upscaled map retains key geological features, including several high-permeability channel-like trends, while smoothing sub-block scale variability — preserving hydraulic continuity critical for flow prediction. Figure 10 illustrates the spatial distribution of predicted CO_2 injection rates for every potential well-block in the interval by layer (Figure 10a) as well as aggregated over all the layers (Figure 10b). Figure 10a reveals strong spatial correlation with the underlying reservoir properties, confirming that the predicted rates are closely related to the geological heterogeneity of the layer. While the majority of the layer exhibits low injectivity (< 0.01 Mt/yr), there are distinct corridors of elevated injection capacity, often associated with high-permeability features and structurally open compartments. In contrast, regions adjacent to sealing faults or dominated by low-permeability facies do not provide good potential injection sites.

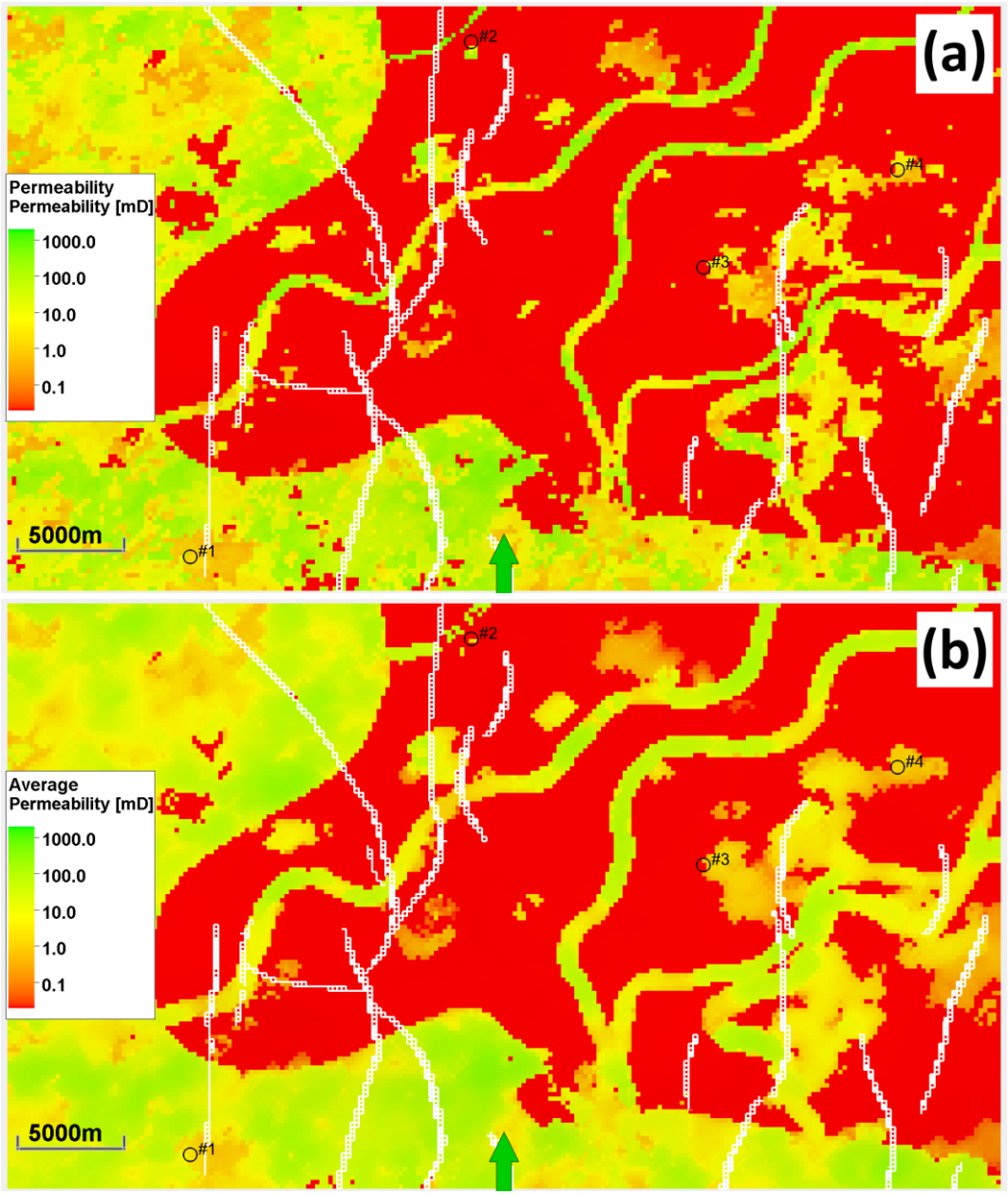

Figure 9 Permeability distribution in an example layer of a regional-scale 3D geological model. (a) Original horizontal permeability extracted directly from the static model. (b) Upscaled permeability computed using the proposed radial averaging method, applied locally within each well-centred region. The upscaled map retains key geological features such as high-permeability channels and barriers, while reducing small-scale variability to enable physically consistent injectivity prediction. White lines represent sealing faults that segment the model into independent compartments. Four out of the twenty test wells are located within this interval and are marked on the maps.

To assess the full injectivity potential of the entire interval, Figure 10b shows the aggregated mass injection rate, computed by summing the block-level predictions vertically across all 28 layers along each (i, j) column. This interval-scale map highlights key injection corridors with cumulative rates exceeding 1 Mt/yr in several locations, providing high-resolution insight into well siting options and subsurface connectivity. The contrast between Figure 10a and Figure 10b underscores the importance of

accounting for vertical stacking of permeable units when evaluating injection feasibility in multi-layered saline aquifers or depleted formations.

Overall, these results demonstrate that the proposed method can resolve both fine-scale heterogeneity and large-scale injection trends with high computational efficiency — enabling basin-scale screening of potential CO_2 storage sites across hundreds of thousands of locations.

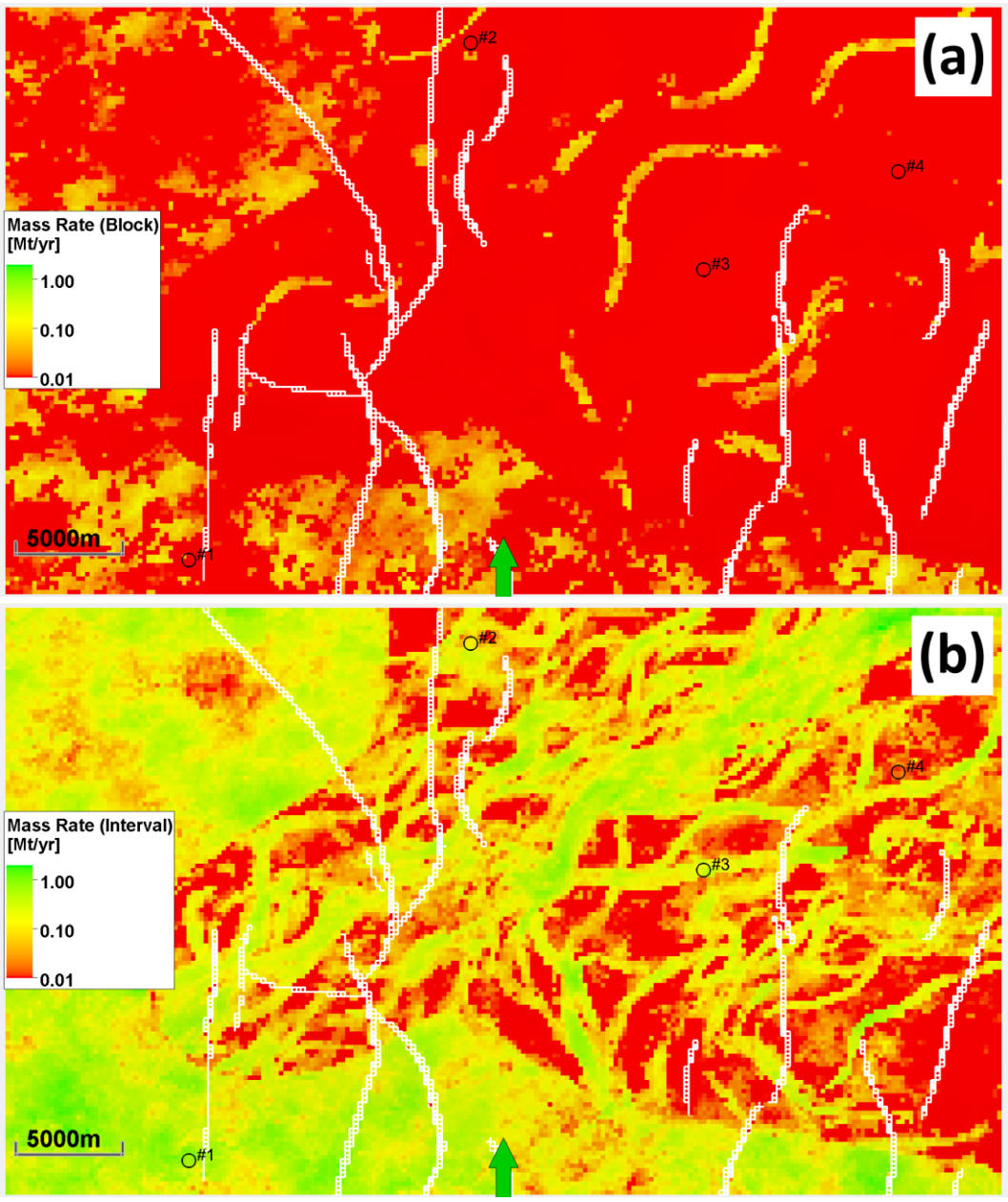

Figure 10 Predicted CO_2 injection rates based on the proposed analytical method applied to a regional-scale 3D geological model. (a) Layer-wise distribution of mass injection rate (Mt/year) for a single representative layer within one selected interval. (b) Total mass injection rate map for the same interval, obtained by summing the contributions of all layers along each ij column. Results reflect the influence of local permeability, compartmentalisation, and fault boundaries on spatial injection capacity. Four out of the twenty test wells are located within this interval and are marked on the maps.

To further evaluate the impact of the proposed radial upscaling method, statistical comparisons were performed between the original and averaged permeability fields across the full regional model (excluding cells associated with non-reservoir facies, such as coals, which were assigned extremely low values). The original permeability distribution is highly heterogeneous, spanning over seven orders of magnitude (from 0.0001 mD to 2000 mD), with a mean value of 15.9 mD and a standard deviation of 52.0 mD. This reflects the geological complexity of the system, including interbedded channelised and low-energy facies. After applying the radial averaging scheme, the resulting distribution remains broad but becomes more centralised, with the maximum value reduced to approximately 911.8 mD, a lower mean of 12.1 mD, and a substantially reduced standard deviation of 31.1 mD. These changes reflect the dampening effect of radial averaging on extreme permeability contrasts, particularly the down-weighting of isolated high-permeability features. The resulting field is smoother and more representative of the effective transmissibility near injection wells, enabling more physically realistic injection rate predictions across highly variable geological settings. This effect is illustrated in Figure 11, which shows the frequency distribution of the averaged permeability field. Compared to the original, the smoothed histogram exhibits a narrower spread and more centralised profile, reflecting the mitigation of extreme contrasts by the radial upscaling method.

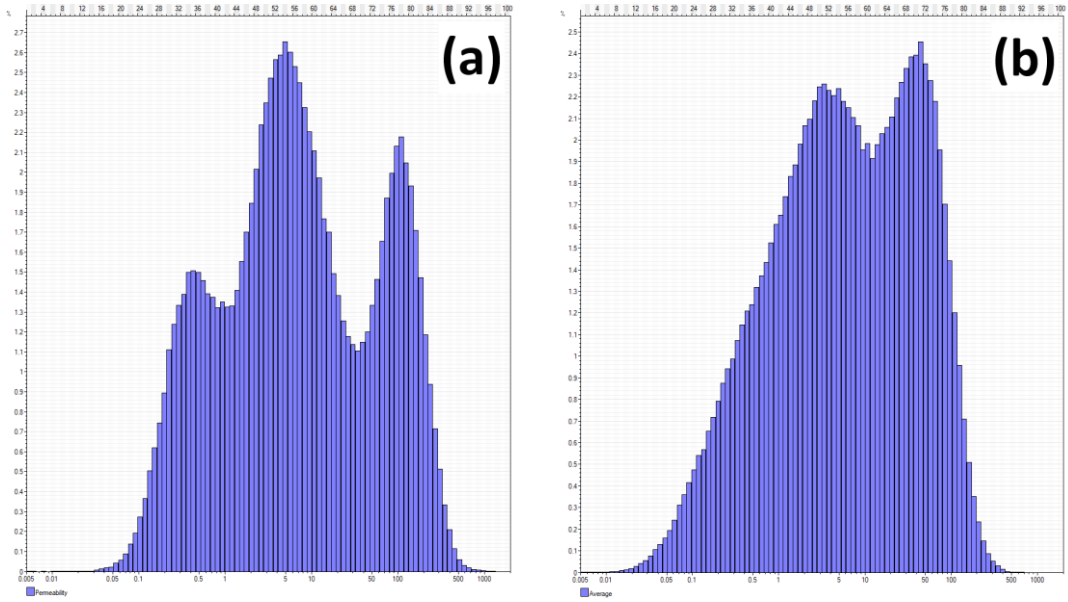

Figure 11 Frequency distributions of horizontal permeability in the regional model before and after radial averaging. (a) Original permeability field extracted from the static geological model, showing a highly heterogeneous distribution spanning over seven orders of magnitude. (b) Upscaled permeability field generated using the proposed radial averaging method, which smooths extreme values while preserving geological trends.

Figure 12 presents a quantitative comparison of the predictive accuracy, specifically showing the absolute percentage error in the injection rate calculated at 20 test locations. The errors are shown for two analytical methods: (i) the analytical upscaling and workflow described in section 2.3 and (ii) the same workflow but with permeability averaged using the method of Soeriawinata et al. (1997). The errors for both methods are calculated relative to the empirically corrected full-physics simulation using CMG-

GEM, which serves as the reference benchmark. All results were converted to mass injection rates (Mt/year) using a standard CO_2 density of 1.857 kg/m^3. Across the 20 cases, the proposed method exhibited significantly closer agreement with numerical simulation results, while the Soeriawinata-based approach consistently underestimated injection rate. To ensure a fair comparison, systematic correction factors derived from homogeneous benchmark cases was independently applied to the numerical simulation results prior to evaluating each analytical method. After this adjustment, the average prediction error of the proposed method 12.7%, with a maximum deviation of 30.1 Under identical conditions, the Soeriawinata et al.'s approach exhibited larger and more systematic errors, with an average and maximum error of 21.8% and 75.8%, respectively., with a lower R^2 value (0.9389) compared to our method (0.9715). As their approach only replaces the permeability averaging step (Steps 2–3), the remainder of the workflow remained identical. Despite its more complex mathematical formulation, their method delivered less accurate predictions than the simpler and more scalable radial averaging proposed here.

These results confirm that the proposed method can be successfully applied to large, geologically realistic 3D models, accounting for structural complexity, permeability heterogeneity, and realistic fluid behaviour. Its ability to deliver accurate mass-based injection rate estimates without reliance on dynamic simulation underscores its suitability for high-throughput screening of candidate injection sites across basins or regions.

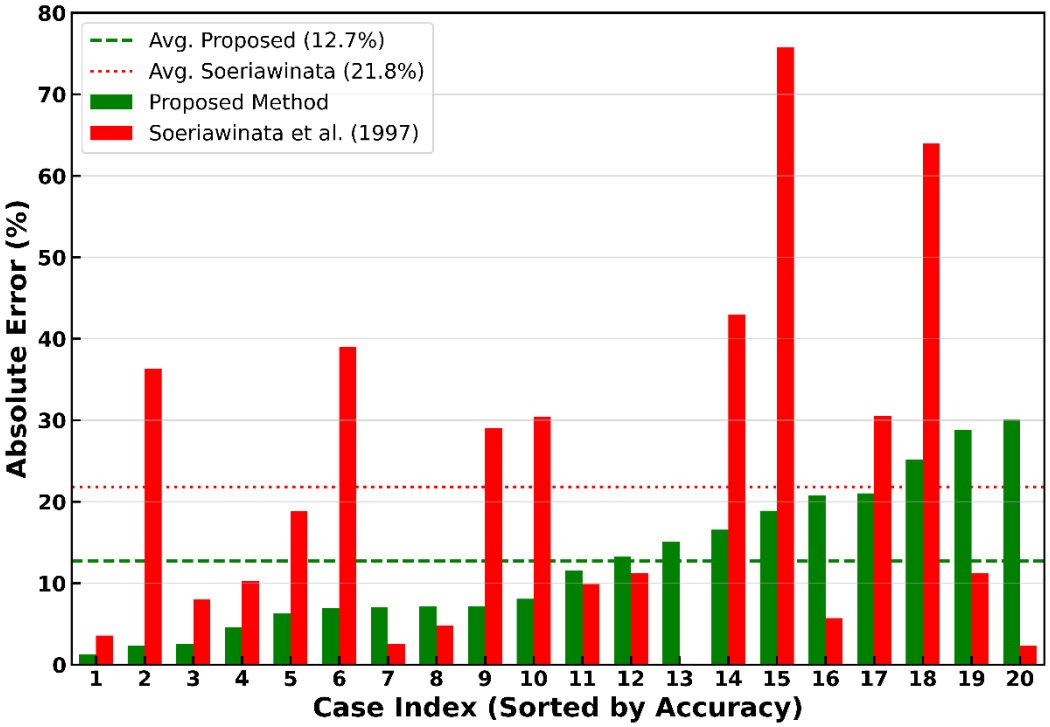

Figure 12 Comparative Absolute Error in Injection Rate Prediction. Absolute percentage error for the proposed analytical method (green bars) compared against the method of Soeriawinata et al. (1997) (red bars) across 20 test cases from a regional 3D geological model. The numerical simulation (CMG-GEM) results used as the reference benchmark were empirically corrected for grid-related artifacts established during homogeneous validation tests. The cases on the x-axis are indexed and sorted by the ascending error of the proposed method to

clearly illustrate performance. The figure demonstrates that the proposed radial averaging technique consistently yields significantly lower absolute error, confirming its superior predictive accuracy for rapid screening applications.

4.3. Runtime and Computational Efficiency

The proposed workflow was applied across all potential injection sites in the regional model, and the subset of test wells was chosen post hoc for focused comparison. To assess the scalability and computational feasibility of the proposed injection rate prediction workflow, the method was applied to the full 3D regional geological model described in section 4 covering an area of ~1,200 km^2 consisting of 226 × 133 × 230 grid blocks, totalling approximately 6.91 million active cells. These blocks correspond to 270,522 unique injection spots (i.e. ij-columns within each stratigraphic interval), where mass injection rates were estimated individually before aggregating the results.

The entire workflow, as shown in Figure A-1, was executed on a high-performance workstation equipped with an Intel® Core™ i9-13900K processor (24 cores), 128 GB of RAM, and Windows 11 Enterprise. The process was run in MATLAB with parallel execution enabled where possible. The total runtime for processing all 270,522 potential injection sites was approximately 274.10 seconds (around 4.5 minutes). Table 3 summarises the breakdown of runtime across each step of the workflow.

Table 3 Runtime breakdown of each step in the proposed injection rate prediction workflow, executed on a high-performance workstation with 128 GB RAM and a 13th Gen Intel® Core™ i9-13900K processor. Parallel computing options in MATLAB were enabled where applicable.

Step	Description	Runtime (s)
1	Data import and pre-processing	5.12
2	Determine weight factors	0.01
3	Radial permeability upscaling	190.18
4	Determine fluid properties locally	61.95
5	Compute mass injection rate	6.26
6	Aggregate block-level results (along ij columns)	0.08
7	Export results	10.49
	Total	**274.10**

Steps 3 and 4 — corresponding to permeability upscaling and fluid property evaluation — represented the most computationally intensive stages. Nonetheless, the total runtime remained under five minutes for the full regional model, validating the method's suitability for large-scale, high-resolution screening applications.

This level of efficiency provides a substantial advantage over detailed dynamic simulations. For conventional full-physics simulation, estimating the injection capacity of a single well location (i.e. a single ij-column within an interval) can require approximately 7-8 hours on the same computational resources, especially when accounting for model setup, fluid property calibration, and run-time convergence. For a full regional model with over 270,000 potential injection spots (i.e. 226 × 133 potential locations per interval across 9 stratigraphic intervals), such an approach becomes computationally prohibitive — potentially requiring years of cumulative runtime, not

including the overhead of preparing and validating thousands of separate simulation inputs.

In contrast, the proposed analytical workflow performs all rate predictions in a single integrated run, while still incorporating essential physical features such as spatial permeability variability, pressure-dependent fluid properties, and stratigraphic layering. This enables consistent, rapid, and physically grounded screening of CO_2 storage potential across regional basins or entire portfolios of candidate sites.

5. Conclusions and Broader Implications

This study demonstrates that rapid, physics-based prediction of pressure-constrained CO_2 injection rates can be achieved in large and geologically complex geological models without the need for fine-grid, detailed simulation. Central to the workflow is a radial permeability averaging scheme that captures near-wellbore heterogeneity and provides an effective permeability suitable for coarse-grid screening analyses.

The workflow also incorporates a geomechanically consistent treatment of safe injection pressure. The maximum allowable pressure at each location is determined from formation strength, overburden stress, and pore pressure, with the permissible pressure increase limited to 90% of fracture pressure in line with EPA Class VI guidance. This ensures that predicted injection rates remain both operationally realistic and compliant with established regulatory safety criteria.

The method was tested on both synthetic cases and a full 3D, geologically consistent regional model with 230 layers, and full facies-constrained porosity and permeability distribution covering an area of ~1,200 km^2 and depth range of ~1,250-2,400 m TVDss. The numerical model contains over 6.9 million cells and 270,000 potential injection sites. The results show strong agreement with CMG-GEM simulations, with an average error of ~12.7% and a maximum error of ~30.1%, while completing the full screening computation in under 5 minutes using parallelised MATLAB routines. Key implications of this work include:

- The workflow bridges the gap between full-physics detailed simulation and rapid analytical screening, enabling basin-scale assessments within minutes.
- The method's robustness across heterogeneous and compartmentalised systems supports its integration into early-stage storage site ranking workflows.
- The approach provides a transparent, physics-grounded foundation that can be adapted for hydrogen, natural gas, or geothermal injection analysis.

6. Acknowledgements

The authors gratefully acknowledge PETRONAS Sdn. Bhd. for supporting this research through the DSALT project (Dynamics of Saline Aquifers over Long Time-scale). The authors also thank Schlumberger and Computer Modelling Group (CMG) for providing software access and technical resources that facilitated parts of the analysis.

Additionally, the authors acknowledge the use of MATLAB® and parallel computing features developed by MathWorks Inc., which enabled efficient implementation and execution of the screening workflow. Their contributions are sincerely appreciated.

Appendix A: Step-by-Step Workflow for Injection Rate Prediction

Each step of the process is outlined below and the overall workflow is visualised in the accompanying flowchart (Figure A-1). While the diagram presents the sequence linearly, in practice Steps 2–5 are repeated in a loop for each potential injection location across the domain. The goal is to screen thousands or millions of possible sites, allowing rapid identification of injection sweet spots across large and geologically complex regions.

1. Data import and pre-processing: Pressure, temperature, permeability, thickness, segment IDs, and other relevant inputs are imported. This could be from Petrel-exported files or other static modelling software. The maximum injection pressure is assigned. This could be the maximum safe pressure using a geo-mechanical constraint or the maximum pressure associated with the facilities. Undefined cells are automatically identified and excluded based on flagged values. This step needs to be performed only once.
2. Determine weight factors: Logarithmic weight factors are computed based on radial distance bins surrounding each injection location via Eq. 7. If the model has uniform lateral grid spacing, a fixed wellbore radius for all wells, and a constant k_y/k_x ratio across the domain, this step may be performed once and reused across all locations. Otherwise, it is repeated per site.
3. Radial permeability upscaling: The effective near-wellbore permeability is calculated using a distance-weighted harmonic average, as defined in Section 2.3. This step (and the ones that follow) are repeated for each valid injection spot.
4. Determine fluid properties for each well-block based on local pressure and temperature.
5. Compute the mass injection rate: Using the pressure-dependent properties and the maximum allowable injection pressure, the mass injection rate is computed for each block using the pseudo-pressure-based transient model. The full integral form is solved, with optional use of the pressure-squared approximation where justified.
6. Aggregate block-level results: Block-level injection rates are summed along the vertical direction (k-axis) for each (i,j) column and stratigraphic interval. Although block-level rates are summed vertically, gravity effects are already accounted for because each block's injection rate is calculated using depth-specific initial and maximum allowable pressures; the summation simply aggregates these depth-adjusted rates across the interval. This effectively reduces the 3D problem to a 2D map of injection potential. If perforations are not assumed across the full interval thickness, unperforated cells can be excluded via zero multipliers.

7. Export results: The final mass-based injection rates (in Mt/yr), along with relevant diagnostic parameters, are exported to support integration with geological characterisation, mapping, and visualisation workflows. Cells previously flagged as undefined (e.g. due to pinch-outs or inactive zones) remain excluded from the output to preserve structural consistency. This step needs to be performed only once.

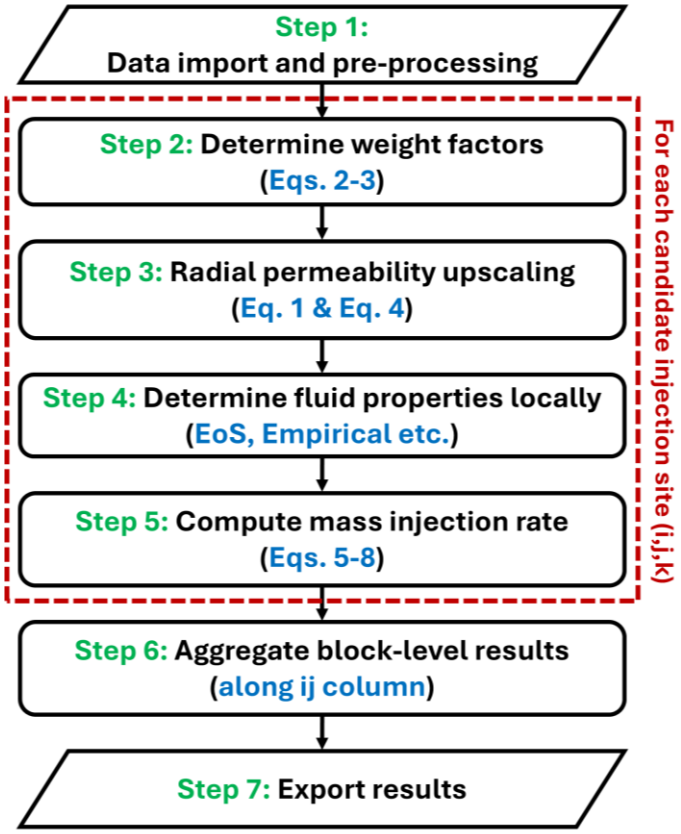

Figure A-1 Schematic workflow for rapid injection rate prediction based on radial permeability upscaling, pressure-dependent fluid properties, and transient flow modelling. The process operates on 3D static models and is designed for efficient application to large-scale CO_2 storage screening. The process operates on 3D static models and is designed for efficient application to large-scale CO_2 storage screening. While presented linearly, Steps 2–5 are internally looped for each injection location across the domain. Equations used in each step are referenced in parentheses.

The workflow is modular by design, allowing users to replace or adapt individual components as required — for example, applying alternative equations of state, viscosity correlations, or relative permeability functions. Although this study focuses on CO_2 injection, the same framework can be readily applied to other injection scenarios, such as hydrogen storage or wastewater disposal.

7. References

Ali, E., Hadj-Kali, M. K., Mulyono, S., Alnashef, I., Fakeeha, A., Mjalli, F. & Hayyan, A. 2014. Solubility of CO2 in deep eutectic solvents: Experiments and modelling using the Peng–Robinson equation of state. *Chemical Engineering Research and Design,* 92**,** 1898-1906, https://doi.org/10.1016/j.cherd.2014.02.004.

Birkholzer, J. T. & Zhou, Q. 2009. Basin-scale hydrogeologic impacts of CO2 storage: Capacity and regulatory implications. *International Journal of Greenhouse Gas Control,* 3**,** 745-756, https://doi.org/10.1016/j.ijggc.2009.07.002.

Celia, M. A., Bachu, S., Nordbotten, J. M. & Bandilla, K. W. 2015. Status of CO_2 storage in deep saline aquifers with emphasis on modeling approaches and practical simulations. *Water Resources Research,* 51**,** 6846-6892, https://doi.org/10.1002/2015WR017609.

Dake, L. P. 1983. *Fundamentals of reservoir engineering*, Elsevier.

Dall'Acqua, D., Terenzi, A., Leporini, M., D'Alessandro, V., Giacchetta, G. & Marchetti, B. 2017. A new tool for modelling the decompression behaviour of CO2 with impurities using the Peng-Robinson equation of state. *Applied Energy,* 206**,** 1432-1445, https://doi.org/10.1016/j.apenergy.2017.09.118.

De Silva, P. N. K. & Ranjith, P. 2012. A study of methodologies for CO_2 storage capacity estimation of saline aquifers. *Fuel,* 93**,** 13-27, https://doi.org/10.1016/j.fuel.2011.07.004.

Ding, D. 2004. Near-well upscaling for reservoir simulations. *Oil & gas science and technology,* 59**,** 157-165, https://doi.org/10.2516/ogst:2004012.

EPA. 2010. *GENERAL TECHNICAL SUPPORT DOCUMENT FOR INJECTION AND GEOLOGIC SEQUESTRATION OF CARBON DIOXIDE: SUBPARTS RR AND UU* [Online]. U.S. Environmental Pretection Agency. Available: https://www.epa.gov/uic/class-vi-wells-used-geologic-sequestration-carbon-dioxide [Accessed Access-Date].

Ertekin, T., Abou-Kassem, J. H. & King, G. R. 2001. *Basic applied reservoir simulation*, Society of Petroleum Engineers.

Hajiabadi, S. H., Bedrikovetsky, P., Borazjani, S. & Mahani, H. 2021. Well Injectivity during CO2 geosequestration: a review of hydro-physical, chemical, and geomechanical effects. *Energy & Fuels,* 35**,** 9240-9267, https://doi.org/10.1021/acs.energyfuels.1c00931.

Krevor, S., De Coninck, H., Gasda, S. E., Ghaleigh, N. S., de Gooyert, V., Hajibeygi, H., Juanes, R., Neufeld, J., Roberts, J. J. & Swennenhuis, F. 2023. Subsurface carbon dioxide and hydrogen storage for a sustainable energy future. *Nature Reviews Earth & Environment,* 4**,** 102-118, https://doi.org/10.1038/s43017-022-00376-8.

Lake, L. W. 1989. Enhanced oil recovery.

Naghizadeh, A., Larestani, A., Amar, M. N. & Hemmati-Sarapardeh, A. 2022. Predicting viscosity of CO2–N2 gaseous mixtures using advanced intelligent schemes. *Journal of Petroleum Science and Engineering,* 208**,** 109359, https://doi.org/10.1016/j.petrol.2021.109359.

National Institute of Standards and Technology (NIST). NIST Chemistry WebBook, SRD 69 [Online]. U.S. Department of Commerce. Available:

https://webbook.nist.gov/cgi/inchi/InChI%3D1S/CO2/c2-1-3 [Accessed November 2024].

Nordbotten, J. M., Celia, M. A. & Bachu, S. 2005. Injection and storage of CO_2 in deep saline aquifers: analytical solution for CO_2 plume evolution during injection. *Transport in Porous media,* 58**,** 339-360, https://doi.org/10.1007/s11242-004-0670-9.

Peaceman, D. W. 1983. Interpretation of well-block pressures in numerical reservoir simulation with nonsquare grid blocks and anisotropic permeability. *Society of Petroleum Engineers Journal,* 23**,** 531-543, https://doi.org/10.2118/10528-PA.

Pumjan, S., Long, T. T., Loc, H. H. & Park, E. 2022. Deep well injection for the waste brine disposal solution of potash mining in Northeastern Thailand. *Journal of Environmental Management,* 311**,** 114821, https://doi.org/10.1016/j.jenvman.2022.114821.

Renard, P. & De Marsily, G. 1997. Calculating equivalent permeability: a review. *Advances in Water Resources,* 20**,** 253-278, https://doi.org/10.1016/S0309-1708(96)00050-4.

Sammon, P. H. 1988. An analysis of upstream differencing. *SPE reservoir engineering,* 3**,** 1053-1056, https://doi.org/10.2118/14045-PA.

Smith, M. B. & Montgomery, C. 2015. *Hydraulic fracturing*, CRC press.

Soeriawinata, T., Kasap, E. & Kelkar, M. 1997. Permeability upscaling for near-wellbore heterogeneities. *SPE Formation Evaluation,* 12**,** 255-262, https://doi.org/10.2118/36518-PA.

Xiong, W., Zhang, L.-H., Zhao, Y.-L., Wen, S.-M., Bao, K., Møyner, O. & Lie, K.-A. 2024. Compositional simulation for carbon storage in porous media using an electrolyte association equation of state. *SPE Journal,* 29**,** 3314-3336, https://doi.org/10.2118/219734-PA.

Zhang, Y., Jackson, C. & Krevor, S. 2022. An Estimate of the Amount of Geological CO2 Storage over the Period of 1996–2020. *Environmental Science & Technology Letters,* 9**,** 693-698, https://doi.org/10.1021/acs.estlett.2c00296.